Macromolecules

pubs.acs.org/Macromolecules Article

Kinetics of All-Dry Free Radical Polymerization under Nanoconfinement

Yifan Cheng, Alexandra Khlyustova, Pengyu Chen, and Rong Yang*

Cite This: https://dx.doi.org/10.1021/acs.macromol.0c01534 Read Online

ACCESS | Metrics & More | Article Recommendations | Supporting Information

ABSTRACT: Conformal coating of ultrahigh-aspect-ratio nanostructures with functional polymer thin films is highly desirable in many applications, ranging from biosensing to energy storage. Nevertheless, achieving uniform surface coverage on nanostructures is challenging due to the difficulty of controlling molecular transport and reaction kinetics under nanoconfinement. Here we demonstrated the conformal coverage of ultrahigh-aspect-ratio nanopores by polymer nanolayers deposited using initiated chemical vapor deposition (iCVD) and unraveled the fundamental mechanisms governing the coating growth kinetics under nanoconfinement. A molecular-collision model was developed by using statistical methods and validated by systematic kinetic experiments. The results indicated that nanoconfinement amplified radical–surface collisions, resulting in higher effective radical concentration. The approach for validating the molecular-collision model can be broadly adopted to study vapor-based reaction systems without needing extensive nanofabrication or characterization instruments. Together, the results reported here could improve the control over nanocoating growth during nanostructured material/device fabrications across industries of manufacturing, healthcare, and sustainability.

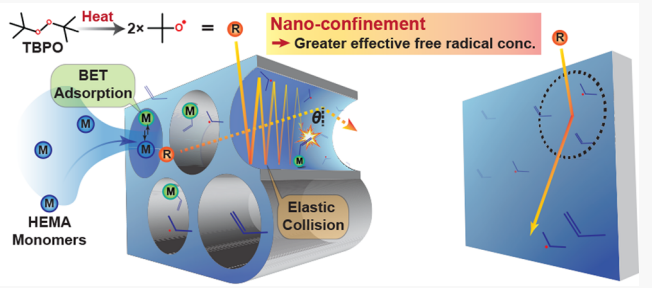

1. INTRODUCTION

Nanostructured substrates with ultrahigh aspect ratios (typically ~10^2 or greater)[1−3] offer unparalleled large surface areas for a fixed device volume and are thus critical in many fields, including membranes used in filtration,[4] (bio)sensors,[5] drug delivery,[6] and energy storage.[7,8] The ability to control their surface properties (e.g., chemistry, surface energy, mechanical properties, and morphology) is therefore key to enabling functions of the aforementioned devices. A common method to control surface properties is surface modification using multifunctional polymer coatings.[9,10] Nevertheless, coating ultrahigh-aspect-ratio nanostructures with uniform polymer nanolayers (defined as coatings with thickness <50 nm)[9] remains a challenge due to the difficulty of controlling transport phenomena and reaction kinetics under nanoconfinement.[11] That is particularly limiting for solution-phase coating methods (e.g., spin/dip coating, inject printing, and layer-by-layer assembly), where the undesirable surface tension effect and the Fickian diffusion mechanism often lead to coating defects and/or nonuniformity.[9]

By avoiding the use of solvents during polymer synthesis and coating process, vapor-based coating techniques, such as initiated chemical vapor deposition (iCVD), have achieved uniform coverage of nanostructured substrates. Indeed, nanopores with aspect ratios as high as 400 and diameters as small as tens of nanometers have been coated conformally by using the iCVD technique.[4] Furthermore, conformal coatings have been applied in a substrate-independent manner onto silicon microtrenches (with aspect ratio <10),[12−14] block copolymer membranes (with aspect ratio <80),[15] self-assembled anodized aluminum oxide (AAO) membranes (with aspect ratios of ~250),[6,16] and track-etched membranes [with aspect ratios approximately $O(10^1)$ to $O(10^2)$].[4,17] Keeping the system in a reaction-limited regime (as opposed to a mass-transfer-limited regime) was found crucial in forming conformal coatings inside nanoporous geometries, eventually achieving complete filling of pores.[18] That tight integration of polymers and inorganic materials has important implications for properties of the composite materials, including polymer glass transition temperature,[19] polymer crystallinity,[20] and specific capacitance.[8]

Both conformal coating and complete filling of pores rely on the arrival of vapor phase reactants to the surface by non-line-of-sight diffusion, i.e., Knudsen diffusion, under modest vacuum conditions and the limited probability of reaction upon a single surface collision.[12,13] Previous studies[4,17] have shown that Knudsen diffusion dominates the mass transport of initiator radicals inside nanoporous substrates due to the

Received: July 2, 2020
Revised: October 9, 2020

micrometer-sized molecular mean free path (λ) under vacuum. Despite that general understanding, the effect of nanoconfinement on the transport of reactants and polymerization kinetics remains unclear. The lack of understanding hindered the precise control of coating growth on nanostructured substrates and thus device fabrication in various applications (e.g., biosensing, drug delivery, and energy storage).

Previous studies done on flat substrates have shown that the rate-determining step in iCVD polymerization is the surface adsorption of monomers, which follows the Brunauer−Emmett−Teller (BET) isotherm.[21,22] Free radical polymerization occurs on the surface upon initiation by vapor-phase radicals via the Eley−Rideal mechanism.[13] Although the precise amount of free radicals is difficult to measure directly (due to their reactive nature), radicals are commonly considered to be in excess; reaction kinetics could otherwise transition to be initiation-limited when that is not the case.[23] That theory of monomer adsorption-limited kinetics has been extended to depositions inside microtrenches (~1 μm wide and 6 μm deep).[12,13] Coating growth kinetics were shown to depend on the sticking probability, Γ (i.e., the probability of a free radical initiating a polymerization reaction upon a surface collision), monomer surface concentration, and aspect ratio of the underlying susbtrates.[12,13] Nevertheless, kinetics of polymerization under nanoconfinement could differ considerably from that inside microstructures (e.g., the microtrenches used in the aforementioned studies) because the Knudsen number (*Kn*, defined as ratio of mean free path to the length scale of the confinement) could be several orders of magnitude greater in nanopores. A detailed understanding is critical for enabling precise control over functional coating thickness and conformality on nanostructured substrates.

Here, we unraveled the effect of nanoconfinement on the deposition rate of polymer coatings and its dependence on the concentrations of monomer and initiator using a porous substrate with ultrahigh-aspect-ratio nanopores. AAO membranes with an average pore diameter of ~200 nm and length of ~55 μm (aspect ratios of ~275) were used as substrates. 2-Hydroxyethyl methacrylate (HEMA, as monomer) and *tert*-butyl peroxide (TBPO, as initiator) were used to deposit poly(2-hydroxyethyl methacrylate) (pHEMA) via iCVD. pHEMA was chosen because it is one of the most widely applied polymethacrylate on nanostructured substrates for applications ranging from biosensing,[6,16] to tissue engineering[24] and controlled drug release.[25] We systematically studied the deposition rate dependency on P_I/P_I^{sat} as well as P_M/P_M^{sat} under ultrahigh-aspect-ratio nanoconfinement and drew comparisons with that on nonstructured surfaces. A collision-based theoretical model was proposed to investigate how incident angles of initiator free radicals, nanoconfinement geometries, and sticking probability collectively influence the trajectories of these free radicals under cylindrical nanoconfinement. Furthermore, the model uncovered how the distribution of the radical-surface collision sites (predicted based on those radical trajectories) can alter the effective concentration of free radicals, and thus the polymer coating growth kinetics, under nanoconfinement. This work provided new fundamental insights into the transport of monomers and initiators and its effect on deposition kinetics under nanoconfinement. These insights could enable the correlation of obscure local deposition conditions under nanoconfinement with bulk gas phase parameters that can be monitored in real time *in situ*. Altogether, the insights provided here could improve control over the growth of polymer coatings on nanostructures with ultrahigh aspect ratios, advancing the development of miniaturized devices in manufacturing, healthcare, and sustainability.

2. EXPERIMENTAL SECTION

2.A. ICVD Depositions. All iCVD films were deposited in a custom-built cylindrical vacuum reactor (Sharon Vacuum Co. Inc., Brockton, MA). *tert*-Butyl peroxide (Sigma-Aldrich, 98%) and 2-hydroxyethyl methacrylate (Sigma-Aldrich, ≥99%) were used as-purchased without further purification. iCVD depositions were performed at five P_M/P_M^{sat} levels (0.12, 0.23, 0.33, 0.43, and 0.56) crossing five P_I/P_I^{sat} (0.002, 0.003, 0.004, 0.005, and 0.007), in total 25 deposition conditions. The chamber pressure was maintained at 350 mTorr and the stage temperature 30 °C. The total flow rate was maintained at 0.68 sccm; in the case of insufficient flow from HEMA and TBPO, argon gas was supplied. For each deposition, an anodized aluminum oxide (AAO) membrane with nominal pore diameter ~200 nm and thickness ~55 μm (WhatmanAnodisc inorganic filter membrane, Maidstone, UK) was placed alongside a Si wafer substrate (type: P/Boron ⟨100⟩, Purewafer, San Jose, CA) on the reactor stage. The edges of these samples were affixed to the reactor cooling stage with Kapton tapes to ensure effective heat conduction. To control deposition of the 100 nm thick pHEMA film on Si wafers for the kinetics experiments, *in situ* monitoring of film growth was performed on a Si wafer by using interferometry with a HeNe laser source (wavelength = 633 nm, JDS Uniphase).

2.B. Topographical Characterization of Substrates. The topography of the top surface of Si wafer and AAO substrate was characterized by using atomic force microscopy (Asylum MFP-3D, Goleta, CA) in AC mode, with n^+-Si PPP-NCSTR-10 tips (resonance frequency ~180 kHz; tip height 10−15 μm; Nanosensors, Neuchâtel, Switzerland). Top-view and cross-sectional images of the pristine AAO and pHEMA-coated AAO were acquired by using scanning electron microscopy with an electron beam energy 1−3 keV (Zeiss Gemini 500, Oberkochen, Germany) after coating the samples with ~2 nm iridium to reduce charging. To prepare cross sections of pHEMA-coated AAO membranes for SEM imaging, these samples were immersed in liquid nitrogen for 10 min to make the polymer layer brittle before snapping the AAO membranes. The pore diameter (D) and areal porosity (φ_s) of the AAO membranes were determined based on the top-view SEM images, and pore length (L) and thickness of the pHEMA coatings based on the cross-sectional images. All image analyses were performed in ImageJ (version 1.52a).[26]

2.C. Film Thickness Determination. The film thickness on flat Si wafer substrates was measured postdeposition by a J.A. Woollam VASE spectroscopic ellipsometer (Lincoln, NE) using 190 wavelengths from 315 to 718 nm at three different incidence angles (65°, 70°, and 75°).[27] A Cauchy−Urbach model was used for data fitting. FTIR measurements were performed to characterize the deposited film on the Si wafer. The average film thickness deposited on the nanopore walls within the AAO membranes was determined by using the "weight method", as described previously.[15] Briefly, weight gain due to the polymer film deposited on an AAO membrane was measured gravimetrically and converted to the volume change using the density of pHEMA (1.274 g cm^{-3}).[25] That volume change was then divided by the total exposed surface area (A_{exp}) of the AAO membrane [$\sim O(10^3)$ cm^2] to derive the *average* film thickness within nanoconfinement. For the weight method calculations, the membrane pores were assumed cylindrical. A_{exp} was calculated by summing the total area of the cylindrical pore walls (A_{pw}) and the nonporous area of the AAO top surface (A_{np}); the area of the AAO bottom, which was in close contact with the cooling stage, was excluded from the exposed area calculation due to limited access to reactive species. See the Supporting Information for more details about the derivation of A_{exp} and the corresponding error propagation analysis.

2.D. Gaussian Process Regression (GPR). To display and analyze the experimentally acquired deposition kinetics data set in 3D with low bias, GPR was conducted on DR_{norm} by using P_M/P_M^{sat} and

https://dx.doi.org/10.1021/acs.macromol.0c01534
Macromolecules XXXX, XXX, XXX−XXX

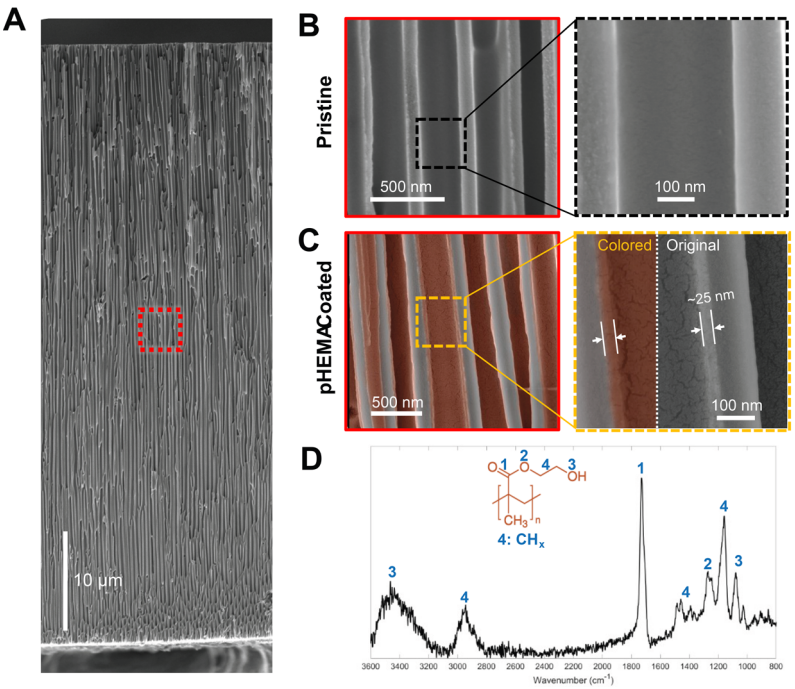

Figure 1. Ultrathin pHEMA coatings along the nanopores of AAO membranes. (A) SEM image showing the entire cross section of an uncoated AAO membrane. (B, C) SEM images of greater magnifications, taken at the midpoint (indicated by the red boxes, which were ~27.5 μm from the top surface) of (B) a pristine AAO membrane and (C) a pHEMA-coated AAO membrane. (D) FTIR spectrum of pHEMA deposited via iCVD. The functional groups of pHEMA were numbered to label the FTIR peaks with the respective moieties.

P_I/P_I^{sat} as predictor variables (i.e., features). To train the model, we used a training set that consisted of 40 data points, each comprising P_M/P_M^{sat}, P_I/P_I^{sat}, and DR_{norm} values acquired experimentally (via iCVD depositions at prespecified conditions). The detailed mathematical formula and algorithms for GPR have been published elsewhere.[28] Briefly, the covariance matrix was computed by using radial basis function (RBF) kernels, and the hyperparameters of the kernels were optimized by minimizing the negative log marginal likelihood. The same GPR procedures were also performed on DR_{pore} to produce interpolated $DR_{pore}-P_I/P_I^{sat}$ curves in 2D. These curves were used to numerically recreate the characteristic turning point of $DR_{norm}-P_I/P_I^{sat}$ curves as quantitative confirmation of the validity of the collision-based model. All GPR computation was performed by using the statistical software R (version 1.2.1335), with the CRAN package "gptk".

2.E. Development of the Collision-Based Model. The collision-based model for free radicals was developed and executed by using statistical software R (version 1.2.1335).

3. RESULTS AND DISCUSSION

3.A. Nanopores with Ultrahigh Aspect Ratios in AAO Membranes. The surface topography and pore structures of commercial AAO membranes were characterized by using atomic force microscopy (AFM) and scanning electron microscopy (SEM). A silicon (Si) wafer was characterized in parallel to highlight the nanostructures of AAO membranes.

Consistent with the reported morphology, the AAO membranes used here had cylindrical pores perpendicular to the membrane surface, with measured average pore diameter = 211 ± 12 nm, pore length = 57.6 ± 1.7, and areal porosity = 38 ± 3% (mean ± standard deviation; N = 4).[29] Based on the average pore diameter and pore length, the average aspect ratio of the AAO pores was calculated to be 273 ± 18. These correspond to a total exposed surface area = (2.2 ± 0.1) × 10^3 cm^2 per membrane, with a relative uncertainty of ~6% (see the section "Error propagation analysis on DR_{pore}" in the Supporting Information for a detailed calculation). The root-mean-square (RMS) roughness of AAO membranes was 47.20 ± 5.81 nm, which only accounted for the topmost section (~200 nm thick) of the nanopores accessible by the AFM cantilever. Nevertheless, that RMS roughness was much greater than that of Si wafers (Figure S1B,D, 0.25 ± 0.10 nm). Despite the minor irregularities in pore size/shape near the top surface of the AAO membranes (Figure S2, top panel), the bulk of the nanopores (i.e., deeper than ~300 nm from the top membrane surface, accounting for >99.5% of the total pore length) was smooth and straight (Figure S2, bottom panel; Figure 1), validating the assumption of cylindrical nano-confinement made during model development later on (see section 3.D).

3.B. Ultrathin, Qualitatively Conformal pHEMA Coatings. The iCVD technique was used to deposit pHEMA coatings that uniformly covered the cylindrical nanopores. During a deposition, an AAO membrane was placed alongside a Si wafer on a cooled stage inside a custom-built vacuum reactor. The vaporized monomer (HEMA) and initiator (TBPO) were metered into the reactor, which was kept at 350 mTorr during all depositions. Filament array suspended above the cooled stage was heated resistively to 230 °C, decomposing TBPO molecules into *tert*-butoxy free radicals. The stage was cooled to 30 °C to promote the physisorption of monomer molecules at the material–vapor interface (e.g., the pore walls and top surfaces), where polymerization was initiated upon collision of the free radicals with the adsorbed monomers.

The molecular structure of the iCVD pHEMA thin films was confirmed by using Fourier-transform infrared spectroscopy (FTIR, Figure 1D). The absence of unreacted C═C bonds (1660–1610 cm^{-1}) indicated successful polymerization.[24] The iCVD process ensured high retention of the functional

https://dx.doi.org/10.1021/acs.macromol.0c01534
Macromolecules XXXX, XXX, XXX–XXX

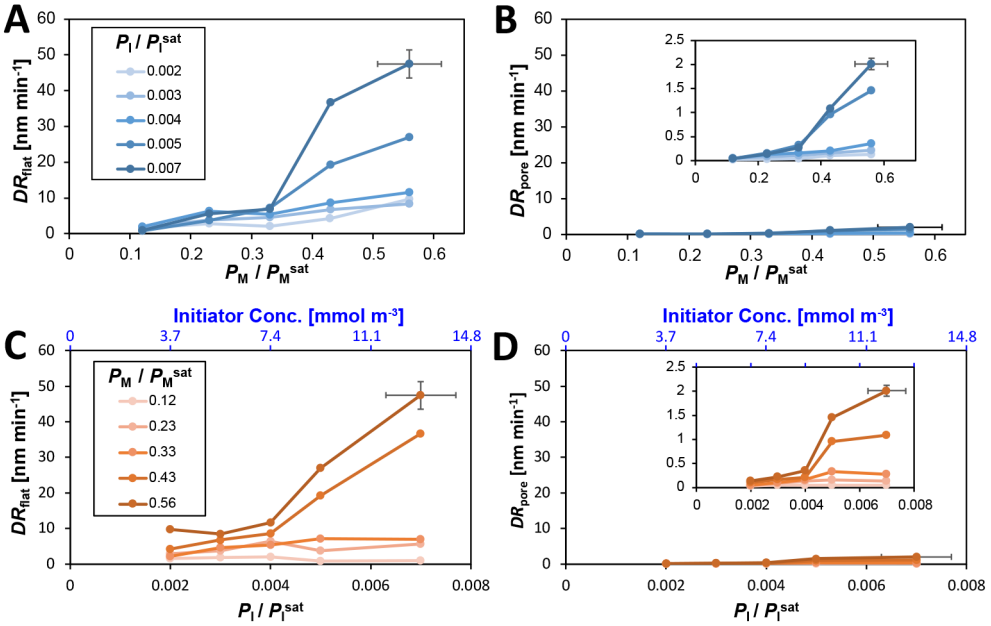

Figure 2. Effect of P_I/P_I^{sat} and P_M/P_M^{sat} on the iCVD deposition kinetics on flat and nanostructured substrates. (A) Rate of deposition on flat substrates, DR_{flat}, and (B) rate of deposition inside nanopores, DR_{pore}, as a function of P_M/P_M^{sat} at fixed P_I/P_I^{sat} values. (C) DR_{flat} and (D) DR_{pore} as a function of P_I/P_I^{sat}, at fixed P_M/P_M^{sat} values. The insets in (B) and (D) are the same data set plotted on magnified *y*-axes. Error bars represent standard deviation (N = 3).

moieties, as evidenced by the broad O−H stretching (3550−3200 cm^{-1}) and out-of-phase C−C−O stretching (primary alcohols, 1075−1000 cm^{-1}) of the hydroxyl groups, strong C═O stretching (1730 cm^{-1}) of the carbonyl groups, and coupled C−O and C−C−O stretching (1270−1240 cm^{-1}) of the ester groups. The peaks were consistent with those reported for vapor- and solution-polymerized pHEMA.[31−33] That high retention of functional moieties during iCVD was a result of the benign nature of this room-temperature process.[9,34]

The deposition left a qualitatively conformal[11] polymer coating inside the nanopores of AAO membranes (Figure 1C, the coating was false colored in brown), meaning that the entire pore wall was coated with a continuous, ultrathin polymer film, up to an aspect ratio of at least ∼205 (depth ∼41 μm), though the coating thickness was found to decrease gradually down the pore (Figure S3). Note that to demonstrate continuous coverage of the pore walls by the pHEMA coating, SEM images of the middle segment of the AAO membranes (∼27.5 μm from the top, highlighted in the red box in Figure 1A) were compared before and after the deposition (Figure 1B,C). In the SEM images, crevices were observed on the pHEMA coating (Figure 1C) but not on the AAO membranes. That was likely a result of the stress cracking of the conductive iridium top coating required for SEM imaging, which is known to occur upon electron radiation due to a mismatch of thermal expansion (between iridium and pHEMA coatings in this case).[35,36]

To our best knowledge, this was the first direct observation of conformal ultrathin iCVD coatings on nanopores with ultrahigh aspect ratios. Although conformal iCVD coatings have been visualized on microtrenches (with width of ∼1 μm and aspect ratios of ∼10),[12,13] the direct observation of ultrathin coatings on nanoscale pores or on structures with such high aspect ratios has not been achieved. Instead, the presence of conformal coatings has been inferred through compositional changes,[4] and/or pore size shrinkage at the topmost surface of membranes,[4,17] and/or by dissolving the nanostructured substrates to image the polymer coating alone.[6]

Here, we demonstrated ultrathin pHEMA coating with thickness measured to be ∼25−30 nm. Notably, that coating thickness within the pores required extended deposition time, during which ∼1500 nm of pHEMA coating was deposited on the Si wafer under the identical deposition conditions. That slower rate of deposition inside nanopores can be ascribed to the overall effect of multiple factors, including substrate temperature, diffusion mass transfer, specific surface area, substrate curvature, and heat of adsorption. We devote the following discussion to the relative contribution of these factors to the rate drop observed in nanopores.

First, to assess the temperature effect, we conducted *in silico* finite element analysis (FEA) along with direct temperature measurement on the top surface of AAO membranes (see the Experimental Section and Supporting Information for details). Both methods independently showed that the AAO membrane was ∼6 °C higher than the Si wafer under our experimental conditions (i.e., T_{stage} = 30 °C, $T_{filament}$ = 230 °C, $P_{reactor}$ = 350 mTorr, and gas flow rate = 0.68 sccm). That higher substrate temperature in turn would result in reduced average adsorption of monomers on the AAO surfaces, thus contributing to the slower DR_{pore}. Nevertheless, this temperature difference would only lead to a $P_{M,Si}^{sat}/P_{M,AAO}^{sat}$ of 0.63 and consequently a DR_{pore}/DR_{flat} of 0.40 [assuming $DR \sim [M]^2 \sim (P_M/P_M^{sat})^2$],[21] which would still be about 1 order of magnitude higher than the observed range of DR_{pore}/DR_{flat} (i.e., 0.01−0.06; see DR_{norm} in Figure 3A,B). Therefore, temperature difference, though confirmed, cannot fully account for the drastic rate drop observed in nanopores.

Next, we turned to the potential effect caused by diffusion mass transfer in nanopores. Under the monomer-adsorption-limited regime (which was the case for deposition on both the flat and the porous substrates),[4,21] the flux of monomer

https://dx.doi.org/10.1021/acs.macromol.0c01534
Macromolecules XXXX, XXX, XXX−XXX

molecules normal to the cooling stage (where AAO membranes and Si wafers were placed) depends on the deposition conditions only; i.e., the same monomer flux can be assumed for AAO membranes and Si wafers. Nevertheless, the nanoporous AAO membrane had a much larger (~400 times) specific surface area than that of the flat Si wafer, thus leading to a much smaller average deposition rate per surface area, which would be roughly inversely proportional to the specific surface area. Note, however, combining the effect of mass transfer with that of the temperature difference leads to a DR_{pore}/DR_{flat} about 1 order of magnitude smaller than the observed range (i.e., ~0.001 vs 0.01). This further necessitates consideration of the effect of the pore wall curvature on monomer adsorption (as described by the Kelvin equation),[37] the difference in the heat of desorption (ΔH_{des}) for the monomers on aluminum oxide vs silicon dioxide,[38] and the effective concentration of initiator radicals under nanoconfinement (discussed in the following sections)—the collective effect of which increases the predicted deposition rate inside AAO nanopores. Quantitative analysis of the aforementioned factors will be an important focus of future studies.

3.C. Decoupled Effects of Monomer and Initiator Concentrations on Polymer Growth Kinetics. To decouple the effects of monomer concentration and initiator concentration, the kinetics of iCVD polymer growth were investigated in two series of experiments: varying monomer concentration at fixed initiator concentrations (blue, Figure 2A,B) and varying initiator concentration at fixed monomer concentrations (orange, Figure 2C,D). See Table 1 for detailed deposition conditions.

As reported previously,[21,22] the concentration of surface-adsorbed monomers was described by P_M/P_M^{sat}, i.e., the ratio of monomer partial pressure in the vapor phase to its saturation pressure at the stage temperature, a first-order approximation of the BET isotherm. The adsorbed monomers are considered to form an apparent monolayer at P_M/P_M^{sat} of ~0.39;[22] the range chosen here (0.12−0.56, Table 1) thus represented surface monomer coverage of <1 monolayer to several monolayers. A similar parameter, P_I/P_I^{sat}, was defined to quantify the surface concentration of initiators. We also calculated the concentration of total initiators (i.e., activated and nonactivated) in the bulk gas phase, using the ideal gas law, as a secondary parameter, which followed the same trend as P_I/P_I^{sat} under constant substrate temperature (see Table 1; Figures 2 and 3, blue labels on top). The P_I/P_I^{sat} range (0.002−0.007, Table 1) was chosen to account for the variety of scenarios ranging from initiation-limited to monomer adsorption-limited reaction kinetics.[22,23,39]

The rate of deposition on Si wafer (i.e., DR_{flat} in Figure 2) was determined by dividing the final coating thickness (determined by using an ellipsometer) on Si wafers by the duration of deposition. The rate of deposition within nanopores (i.e., DR_{pore} in Figure 2) was calculated by using the postdeposition weight gain of AAO membranes and the duration of deposition (see the Experimental Section for details).[15] By using that method, it was assumed that coatings covered the membrane pore walls in a qualitatively conformal manner (i.e., without pore clogging). To test that assumption, we examined the AAO membranes coated by using the highest P_M/P_M^{sat} (i.e., 0.56) and P_I/P_I^{sat} (i.e., 0.007), the deposition conditions that gave rise to the most nonconformal coating.[4,13] Indeed, no pore clogging was identified by SEM (Figure S4) under those conditions. Despite the possible variation in thickness of the iCVD coating along the pores,[4,40] the aforementioned method provides a facile and reproducible way to estimate the *average* rate of deposition over the entire AAO surface area, which is dominated by the internal surface of nanopores (see the section "Validation of the weight method" in the Supporting Information for further details).

Under identical deposition conditions, the rate of deposition on flat substrates (Figure 2A,C), DR_{flat}, was found to be 17−80-fold that under nanoconfinement, DR_{pore} (Figure 2B,D), corroborating the disparity in coating thickness observed on the corresponding substrates. Despite its much smaller values, DR_{pore} followed similar scaling laws as DR_{flat} with respect to the concentrations of monomer at fixed P_I/P_I^{sat} values (insets of Figure 2B); i.e., the rate of deposition increased with P_M/P_M^{sat} monotonically throughout the tested range. That increasing trend was consistent with previous reports.[21,22] Error propagation analysis was then performed to confirm the validity and appropriateness of the weight method employed here for studying iCVD deposition kinetics on porous substrates. To this end, the fastest deposition (conducted under P_M/P_M^{sat} = 0.56 and P_I/P_I^{sat} = 0.007) was performed in triplicate to obtain an upper-bound estimate for the variability in the weight gain of AAO membranes arising from the iCVD process (see Figure 2B,C, data points with error bars representing standard deviations). After propagating variations

Table 1. Experimental Conditions for ICVD Polymerization of pHEMA on Si Wafers and AAO Membranes[a]

monomer[b]		initiator[c]		argon	
P_M/P_M^{sat}	flow rate, F_M (sccm)	P_I/P_I^{sat}	[I] in bulk gas phase (mmol m^{-3})	flow rate, F_I (sccm)	flow rate, F_{Ar} (sccm)
0.12	0.06	0.002	3.70	0.15	0.47
		0.003	5.55	0.21	0.41
		0.004	7.41	0.27	0.35
		0.005	9.26	0.33	0.29
		0.007	12.96	0.52	0.10
0.23	0.11	0.002	3.70	0.15	0.42
		0.003	5.55	0.21	0.36
		0.004	7.41	0.27	0.30
		0.005	9.26	0.33	0.24
		0.007	12.96	0.52	0.05
0.33	0.16	0.002	3.70	0.15	0.37
		0.003	5.55	0.21	0.31
		0.004	7.41	0.27	0.25
		0.005	9.26	0.33	0.19
		0.007	12.96	0.52	0
0.43	0.21	0.002	3.70	0.15	0.32
		0.003	5.55	0.21	0.26
		0.004	7.41	0.27	0.20
		0.005	9.26	0.33	0.14
		0.007	12.96	0.52	0
0.56	0.26	0.002	3.70	0.15	0.27
		0.003	5.55	0.21	0.21
		0.004	7.41	0.27	0.15
		0.005	9.26	0.33	0.09
		0.007	12.96	0.52	0

[a] $T_{substrate}$ = 30 °C, $T_{filament}$ = 230 °C, and $P_{reactor}$ = 350 mTorr for all depositions. [b] Monomer is HEMA; P_M/P_M^{sat} is the ratio of monomer partial pressure in the vapor phase to its saturation pressure at the stage temperature. [c] Initiator is TBPO; P_I/P_I^{sat} is the ratio of initiator partial pressure in the vapor phase to its saturation pressure at the stage temperature.

https://dx.doi.org/10.1021/acs.macromol.0c01534
Macromolecules XXXX, XXX, XXX−XXX

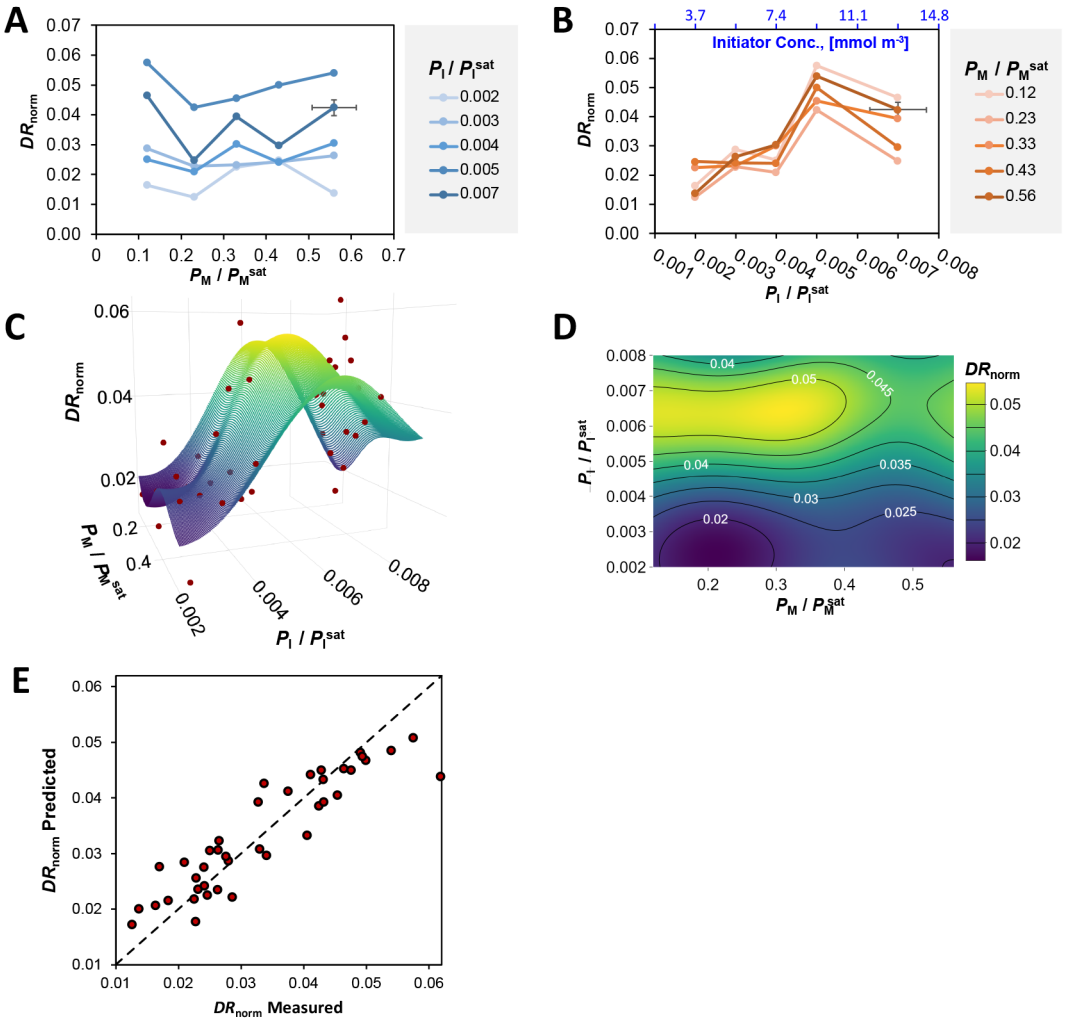

Figure 3. Effects of P_I/P_I^{sat} and P_M/P_M^{sat} on the normalized rate of deposition (DR_{norm}), defined as DR_{pore}/DR_{flat}. (A) DR_{norm} as a function of P_M/P_M^{sat} at fixed P_I/P_I^{sat} levels. (B) DR_{norm} as a function of P_I/P_I^{sat} at fixed P_M/P_M^{sat} levels. (C) Gaussian process regression (GPR) for DR_{norm} in 3D using P_I/P_I^{sat} and P_M/P_M^{sat} as the predictor variables, with red spheres denoting the experimental observations. (D) Corresponding contour plot of the GPR-regressed DR_{norm} response surface, with the contour lines denoting deposition conditions that would result in DR_{norm} with the indicated values; DR_{norm} values in (C) and (D) are represented using the same color scale. (E) Linear correlation between the DR_{norm} predicted by GPR and the values measured experimentally; the dashed line represents the diagonal. Error bars represent standard deviations (N = 3).

of the AAO membrane geometric parameters and variations in the weight gain and deposition time into DR_{pore} (see the Supporting Information for the derivation), the analysis predicted an upper-bound estimate for $\sigma(DR_{pore})$ of ±0.14 nm min^{-1}, or a relative error [i.e., $\sigma(DR_{pore})/DR_{pore}$] of 7.6%. This small error margin affords confidence that the calculated iCVD deposition kinetics are reasonably accurate.

DR_{flat} and DR_{pore} remained constant (at ∼1.40 nm min^{-1} and ∼0.04 nm min^{-1}, respectively) throughout the tested range of P_I/P_I^{sat} when P_M/P_M^{sat} was fixed at the lowest value ∼0.12, indicating polymer chain growth was likely limited by the surface adsorption of HEMA. With P_M/P_M^{sat} of ∼0.23, DR_{flat} and DR_{pore} increased by ∼3.48 nm min^{-1} and ∼0.097 nm min^{-1}, respectively upon increasing P_I/P_I^{sat} from 0.002 to 0.004, and plateaued at ∼5.46 nm min^{-1} and ∼0.14 nm min^{-1} respectively, at P_I/P_I^{sat} > 0.004; similar trends were observed for the dependence of DR_{flat} and DR_{pore} on P_I/P_I^{sat} with the P_M/P_M^{sat} value of 0.33. With P_M/P_M^{sat} value of 0.43, DR_{flat} increased monotonically with P_I/P_I^{sat} throughout the tested range of P_I/P_I^{sat} (i.e., 0.002−0.007), whereas DR_{pore} plateaued at ∼1.02 nm min^{-1} at $P_I/P_I^{sat} \geq$ 0.005. Similarly, with P_M/P_M^{sat} value of 0.56, the rate of increase in DR_{flat} (i.e., the slope) remained mostly unchanged throughout the tested range of P_I/P_I^{sat}, whereas there existed a notable decrease in the slope of DR_{pore} starting at P_I/P_I^{sat} ∼ 0.005. Although this phenomenon was most obvious with P_M/P_M^{sat} values of 0.43 and 0.56, it was also present at lower P_M/P_M^{sat} values—this became evident upon normalizing DR_{pore} with DR_{flat} (see Figure 3B).

To further dissect the effect of nanoconfinement on deposition kinetics, we normalized DR_{pore} by the corresponding DR_{flat} obtained under the same deposition conditions, i.e., $DR_{norm} = DR_{pore}/DR_{flat}$ (Figure 3). This normalization step allowed us to (i) isolate the difference in trends between DR_{pore} and DR_{flat} from their respective trends and (ii) preclude any unknown systematic error in our experimental setup from interfering with data interpretation. Figure 3A shows that DR_{norm} remained largely unchanged as P_M/P_M^{sat} increased, confirming the observation that deposition kinetics followed similar scaling laws with respect to the monomer concentration, regardless of the presence of nanoconfinement. DR_{norm}

https://dx.doi.org/10.1021/acs.macromol.0c01534
Macromolecules XXXX, XXX, XXX−XXX

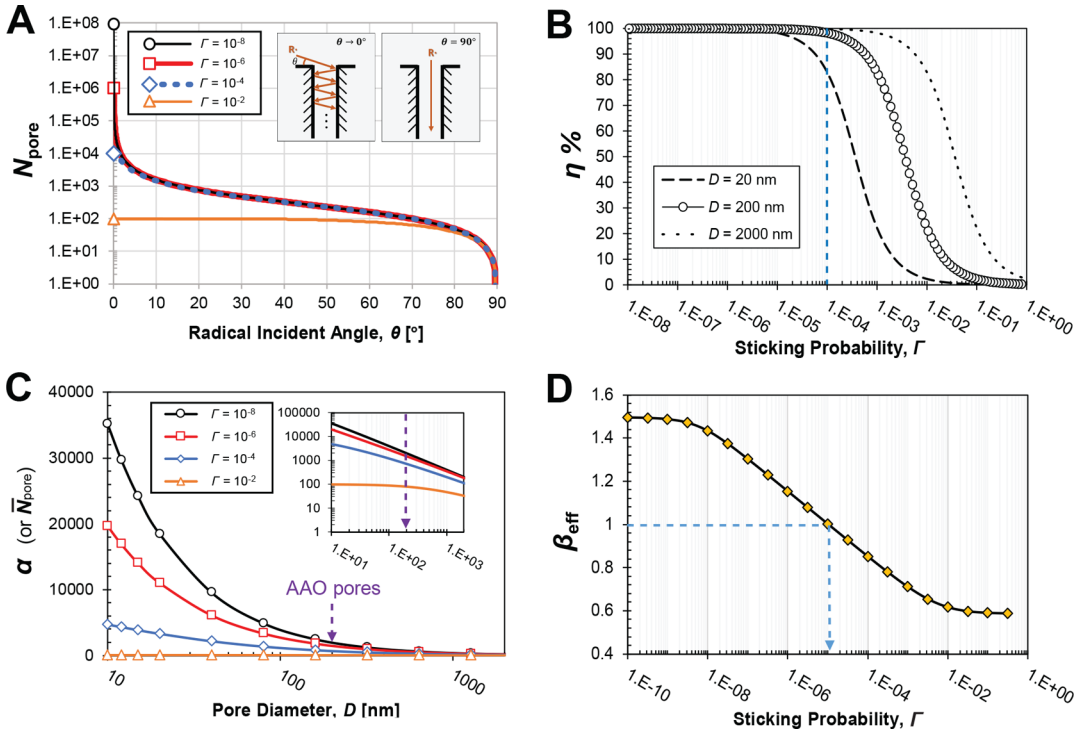

Figure 4. Theoretical model for deposition kinetics under nanoconfinement (at fixed pore length L = 55 μm). (A) Number of radical−surface collisions within a cylindrical nanopore (diameter D = 200 nm), N_{pore}, as a function of radical incident angle, θ, with the sticking probability, Γ, of 10^{-2}, 10^{-4}, 10^{-6}, and 10^{-8}. (B) Proportion of the free radicals (η) that end up exiting without reacting among all the radicals that entered the pores of varying diameters (D = 20, 200, and 2000 nm) as a function of Γ. (C) Collision frequency amplification factor, α, as a function of pore diameter for the aforementioned Γ values (purple arrows indicate the AAO pores used in this work; inset shows the data on a log−log scale). (D) Effective relative areal collision frequency for the AAO membranes, β_{eff}, as a function of Γ, with β_{eff} = 1 achieved at the Γ value of ~10^{-5} (blue dashed lines).

showed an unequivocally consistent correlation with P_I/P_I^{sat}, one that persisted throughout the tested range of P_M/P_M^{sat}, where DR_{norm} increased and then decreased with P_I/P_I^{sat} with an invariable maximum turning point around $P_I/P_I^{sat} \sim 0.005$ (Figure 3B).

The disparate effects of P_M/P_M^{sat} and P_I/P_I^{sat} on DR_{norm} were highlighted by mapping the experimental data onto a 3D space (Figure 3C), with the corresponding contour plot shown in Figure 3D. To further illustrate the data trends, a DR_{norm} response surface was created by applying to the experimental data the Gaussian process regression (GPR, a Bayesian nonparametric regression approach) with radial basis function (RBF) kernels (ensuring low training bias; see the Experimental Section for further details).[28] GPR was chosen because it has been proven effective in fitting nonlinear data sets without assuming any parametrized model function.[28] Applying the GPR also enabled high-fidelity interpolation of the DR_{norm} response surface by using *all* of the experimentally acquired data with their exact P_M/P_M^{sat} and P_I/P_I^{sat} coordinates (denoted by the red dots in Figure 3C); as such, this interpolated response surface further facilitated both hypothesis and model validation (see section 3.E for further details). Indeed, the fidelity of the GPR regression was confirmed by performing a linear correlation between the experimentally obtained DR_{norm} and the values predicted by GPR (Figure 3E). The high correlation coefficient (r = 0.91) indicated that GPR accurately captured the deposition kinetics as a function of both P_M/P_M^{sat} and P_I/P_I^{sat}.

3.D. A Collision-Based Model for the Deposition Kinetics under Nanoconfinement. To better understand the effect of nanoconfinement on deposition kinetics and the strong dependence of DR_{norm} on P_I/P_I^{sat} revealed in Figure 3, a collision-based kinetic model was developed. Inspired by the key observation that concentration of the initiators seems to have a much greater effect than that of the monomers on DR_{norm}, we decided to adopt an initiator-centric perspective, which is distinct from yet complementary to the monomer-centric perspective adopted previously.[4]

To develop the collision-based model, we first assumed that the concept of radical sticking probability applies to ultrahigh-aspect-ratio nanoconfinements; i.e., *tert*-butoxy radicals travel down the nanopores by colliding with pore walls until they react with the surface adsorbed monomers (i.e., "stick"). That sticking probability, Γ, has been estimated to be on the order of 10^{-8}−10^{-2}, depending on surface coverage by the monomers, monomer-initiator reactivity, and aspect ratios of the confinement.[11−13] At a given stage temperature and thus thermal velocity of gas molecules, nanopores lead to a higher frequency of radical-surface collision than microtrenches or flat substrates. The collision-based model developed here provides further insight, in a quantitative manner, into that effect of radical−surface collisions on deposition kinetics under nanoconfinement. The theoretical model was based on the following assumptions: (I) Nanopores are cylindrical with smooth walls. (II) Radical−surface collisions are purely elastic with specular reflection. (III) The model considers the effective concentration of radicals, i.e., only radicals that are not quenched during collisions are included in the model. (IV) The radical sticking probability remains constant while traveling inside nanopores. (V) Only free radicals entering the nanopores in the radial directions were considered, which could lead to an underestimation of the collision frequency.

https://dx.doi.org/10.1021/acs.macromol.0c01534
Macromolecules XXXX, XXX, XXX−XXX

Nevertheless, radicals entering via off-radial trajectories could be analyzed by using the same theories elucidated below.

Based on those assumptions, for a radical that entered a nanopore of diameter D and length L at an incident angle θ, it would either react with surface-adsorbed monomers (i.e., "sticking") or exit the nanopore through the other end. Therefore, the average number of collisions the radical experiences, N_{pore}, can be expressed as (see the Supporting Information for the derivation)

$$N_{pore} = \frac{L}{D \tan\theta}(1-\Gamma)^{N_{max}-1} + \sum_{n=1}^{N_{max}-1} n\Gamma(1-\Gamma)^{n-1} \quad (1)$$

where L is pore length, D the pore diameter, θ the radical incident angle, Γ the sticking probability, n the number of radical−surface collisions before sticking, and N_{max} the maximum number of collisions a radical can have before exiting the pore without reacting:

$$N_{max} = \text{Integer}\left[\frac{L}{D \tan\theta}\right] + 1 \quad (2)$$

Based on eqs 1 and 2, N_{pore} as a function of the radical incident angle, θ, can be calculated (Figure 4A), assuming the nanopore dimensions of D = 200 nm and L = 55 μm (i.e., matching that of an average pore in AAO membranes used). A wide range of Γ values (covering previously reported values ranging from 10^{-8} to 10^{-2})[11−13] was used to capture the effect of Γ on N_{pore}. Intuitively, the free radicals that entered nanopores at smaller incident angles would experience a greater number of wall collisions than those at larger incident angles (two extreme scenarios shown in Figure 4A, insets). At incident angles close to 0°, N_{pore} is close to $1/\Gamma$, and radicals likely end up reacting before exiting the pore (Figure 4A, left inset); at incident angles close to 90°, N_{pore} is independent of Γ because radicals likely exit pores before reacting (Figure 4A, right inset). At intermediate incident angles, radicals could react away or exit pores, depending on the value of Γ. As shown in Figure 4A, the N_{pore}−θ correlations for $\Gamma = 10^{-4}$, 10^{-6}, and 10^{-8} overlap over the entire range of incident angles except for the very small θ (<2°), implying that at Γ values less than 10^{-4} the majority of radicals that have entered the nanopores leave without reacting (i.e., nonreacted). This strikingly high proportion of nonreacted radical population is corroborated by Figure 4B, where proportion of the nonreacted radicals, η, is shown to asymptotically approach 100% as Γ gets smaller (see the Supporting Information for the derivation of η). Figure 4B also shows that η at $\Gamma = 10^{-4}$(marked by the blue dashed line) increases with D at fixed L = 55 μm: from η = 81.9% for D = 20 nm, to η = 98.1% for D = 200 nm, and to η = 99.8% for D = 2000 nm. This positive correlation between η and D can be attributed to the higher maximum number of radical-surface collisions (i.e., N_{max}) − thus increased chance of reacting−for the radicals that have entered a pore of smaller diameters (see eq 2).

Next, the effect of nanoconfinement on deposition kinetics was extracted by first averaging the number of collisions at all incident angles:

$$\bar{N}_{pore} = \frac{2}{\pi}\int_0^{\pi/2} N_{pore}\, d\theta \quad (3)$$

Equation 3 provides the average number of collisions experienced by radicals that have entered the nanopores via radial directions. Assuming the areal density of ρ for radicals impinging on a flat surface (i.e., number of radicals impinging per unit time on a unit area of a flat surface), the average frequency of collisions experienced by the nanopore can be calculated as $\rho\pi(D/2)^2\bar{N}_{pore}$ (i.e., number of collisions per unit time). Similarly, the average frequency of collisions experienced by an equivalent flat surface [i.e., a flat surface with the area of $\pi(D/2)^2$] is $\rho\pi(D/2)^2$, assuming a radical does not impinge on the same area twice given the small cross sections of the nanopores. The collision frequency amplification factor, α, as a result of nanoconfinement, is therefore

$$\alpha \overset{\text{def}}{=} \frac{\rho\pi\left(\frac{D}{2}\right)^2\bar{N}_{pore}}{\rho\pi\left(\frac{D}{2}\right)^2} = \bar{N}_{pore} \quad (4)$$

where $\bar{N}_{pore}$ is angle-averaged number of collisions per free radical (see eq 3), ρ the areal density of radicals impinging on a flat surface, and D the pore diameter. Figure 4C highlights the amplification effect of the nanoconfinement on radical−surface collision frequency: assuming a pore length L of 55 μm (i.e., matching that of the AAO membranes used experimentally), α decreases with increasing pore diameter, achieving values of 80 (at $\Gamma = 10^{-2}$), 707 (at $\Gamma = 10^{-4}$), 1509 (at $\Gamma = 10^{-6}$), and 2253 (at $\Gamma = 10^{-8}$) with D = 200 nm (i.e., pore diameter of the AAO membranes). The model also predicts that pores larger than 500 nm do not have a substantial amplification effect on the number of collisions, which is corroborated by the often smaller Kn values under micro- or larger confinement. Also note Figure 4C only considered D < 2000 nm, which corresponds to Kn > 20 under the experimental conditions, to satisfy the assumption of Knudsen diffusion. Quantitatively, the effect of nanoconfinement strongly depends on the value of sticking probability, Γ. The lowest sticking probability, i.e., $\Gamma = 10^{-8}$, gives rise to the greatest amplification of radical−surface collisions by allowing free radicals to impinge on the surface with low chance of reaction. Compared to a flat surface, an ultrahigh-aspect-ratio nanopore could amplify the radical−surface collisions by 2−3 orders of magnitude; as such, the chance of a radical reacting with the vinyl bond of a monomer or a growing chain end increases considerably. Consequently, the nanoconfinement imposed by the nanopores effectively increased the probability of reaction events for a radical. To further delineate the effect of the amplified radical−surface collisions on reaction kinetics, we need to compare the areal collision frequency under nanoconfinement and that on flat surfaces.

The relative areal collision frequency, β, which removes the effect of the large surface-to-volume ratio associated with nanopores and thus reflects the effect of the nanoconfinement itself, can be calculated as

$$\beta \overset{\text{def}}{=} \frac{\rho\pi\left(\frac{D}{2}\right)^2\bar{N}_{pore}/(\pi DL)}{\rho\pi\left(\frac{D}{2}\right)^2 \Big/ \left[\pi\left(\frac{D}{2}\right)^2\right]} = \frac{D\bar{N}_{pore}}{4L} = \frac{D\alpha}{4L} \quad (5)$$

where $\bar{N}_{pore}$ is the angle-averaged number of collisions per free radical (see eq 3), ρ the areal density of radical impinging on a flat surface, D the pore diameter, and L the pore length.

With D = 200 nm and L = 55 μm, β decreases with increasing Γ, from β = 1.94 at $\Gamma = 10^{-8}$ to β = 0.01 at $\Gamma = 10^{-2}$ (Figure S6). Furthermore, upon removal of the amplification effect caused by the large surface-to-volume ratio of

https://dx.doi.org/10.1021/acs.macromol.0c01534
Macromolecules XXXX, XXX, XXX−XXX

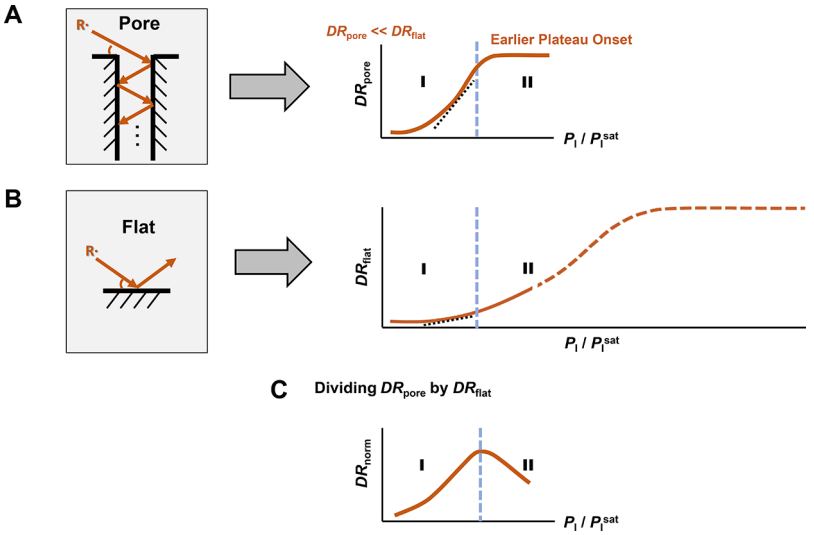

Figure 5. Proposed mechanism for the effect of nanoconfinement on DR_{norm}. (A) Free radicals that have entered a nanoscale pore experience a greater areal frequency of radical−surface collisions than that (B) on a flat surface, which led to the plateau of DR_{pore} at lower P_I/P_I^{sat}. (C) DR_{norm} as a function of P_I/P_I^{sat} has the distinct shape, which is a result of the amplified areal frequency of radical−surface collisions under nanoconfinement.

nanostructures, β decreases as the diameter of the nanopores becomes smaller (eq 5; Figure S6), which is the opposite of the trend for α (Figure 4C). This trend of β suggests that as D decreases, the "dilution" of areal collision frequency by the extremely high surface area outweighs the amplification of α. It is also noteworthy that β can drop below unity, meaning that the average areal collision frequency can be smaller under nanoconfinement than on a flat surface of identical cross-section area, even though the corresponding α is much greater than unity.

Finally, to accurately illustrate the overall effect of a nanoporous substrate, e.g., AAO membranes, the areal porosity (φ_s) was used to calculate the *effective* relative areal collision frequency:

$$\beta_{eff} \overset{def}{=} (1 - \varphi_s) + \varphi_s\beta \tag{6}$$

Using properties of the AAO membranes (D = 200 nm, L = 55 μm, and φ_s = 0.40), we plotted β_{eff} as a function of Γ (Figure 4D). To apply the collision-based theories to the experimental system, the sticking probability of the *tert*-butoxy radical on surface-adsorbed HEMA was estimated to be ~10^{-7}, which was supported by previous theoretical calculations.[11] By use of eq 6, that sticking probability gives the effective relative areal collision frequency of 1.30. Nevertheless, that greater areal collision frequency does not translate directly to faster polymer growth, as (i) the limited transport of monomers inside nanopores could create a descending monomer concentration gradient along the pore length,[4] which is a likely reason for the slower polymer growth inside nanopores; and (ii) a high value of β_{eff} can also lead to primary radical termination,[22] inhibiting the rate of polymer growth. In fact, experimentally, the greater areal collision frequency under nanoconfinement was evidenced by the turning point of the DR_{norm}−P_I/P_I^{sat} curves (Figures 3B and 5; see the next section for further details).

3.E. Quantitative Confirmation of the Validity of the Collision-Based Model. As shown in Figures 2C and 2D, the rate of deposition increased with P_I/P_I^{sat} and plateaued when polymerization transitioned to the monomer-adsorption-limited regime, where the rate of deposition became independent of P_I/P_I^{sat}. As the collision-based theory indicated, nanoconfinement led to greater areal collision frequency that could be viewed as a higher apparent concentration of radicals. That higher apparent radical concentration inside nanopores in turn led to the earlier plateau of DR_{pore} as a function of P_I/P_I^{sat} (Figure 5A) than that of DR_{flat} (Figure 5B). The distinct shape of the DR_{norm}−P_I/P_I^{sat} curves (Figure 3B) hence emerged upon normalization of DR_{pore} by DR_{flat}.

As a quantitative validation of the collision-based model, the effective relative areal collision frequency β_{eff}, which was derived from the model and calculated purely theoretically, was used to recreate the turning point of DR_{norm} as a function of P_I/P_I^{sat} (Figure 3B). Note that the DR_{pore} values plotted in Figure 6 were based on the GPR interpolation (see section 3.C) to ensure that the trend was evident even with limited experimental data points. To recreate the turning point, a theory-corrected curve was generated by plotting DR_{pore} as a function of $[P_I/P_I^{sat}]_{eff}$, the latter obtained by multiplying the corresponding P_I/P_I^{sat} values by β_{eff} (dashed black curve in Figure 6). The β_{eff} value of 1.30 was used here (see section 3.D). The collision-based model predicted that the greater

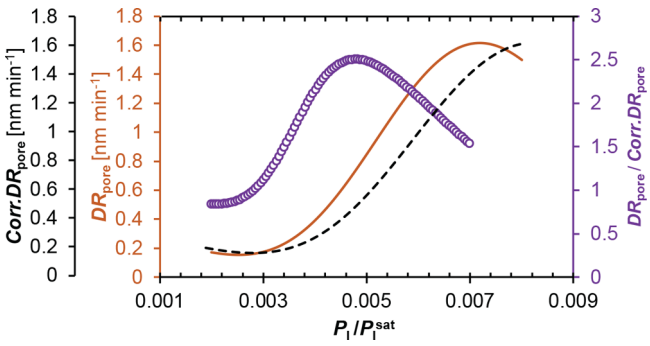

Figure 6. Model validation by recovering the turning point of the DR_{norm}−P_I/P_I^{sat} curve (at P_M/P_M^{sat} = 0.23) by using the theoretical β_{eff} value (β_{eff} = 1.30) calculated via the collision-based model. The characteristic shape of DR_{norm} (purple) was reproduced by dividing the GPR-interpolated DR_{pore} (orange curve) by a theory-corrected curve (black dashed curve), the latter generated by multiplying the corresponding P_I/P_I^{sat} in the orange curve by β_{eff}.

https://dx.doi.org/10.1021/acs.macromol.0c01534
Macromolecules XXXX, XXX, XXX−XXX

effective areal collision frequency (β_{eff}) was the reason for the earlier plateau of DR_{pore} compared to DR_{flat}. Therefore, by accounting for that collision amplification effect, the theory-corrected curve (i.e., DR_{pore} as a function of $[P_I/P_I^{sat}]_{eff}$) should reflect the dependence of DR_{flat} on P_I/P_I^{sat}, albeit the different absolute values for DR_{flat} and DR_{pore}. Thus, the turning point, obtained experimentally to be around P_I/P_I^{sat} of ∼0.005 (Figure 3B), should be recovered if the curve of $DR_{pore}-P_I/P_I^{sat}$ is divided by the $DR_{pore}-[P_I/P_I^{sat}]_{eff}$ curve instead of $DR_{flat}-P_I/P_I^{sat}$. Indeed, that theory-based curve correction yielded an identical turning point, one around P_I/P_I^{sat} of ∼0.005 (purple curve in Figure 6), validating the collision amplification hypothesis. Together, these simulation results lent strong quantitative support for the collision-based model.

3.F. Limitations of the Model and Future Directions. The main purpose of the collision-based model proposed here is to bring to light the intriguing phenomenon—amplification of the effective radical concentration under nanoconfinement. To demonstrate this phenomenon effectively, we have predominantly focused on the *average* coating thickness, which reflects the deposition kinetics, instead of local coating thickness (i.e., conformality). The effect of this amplification phenomenon on conformality, though important, is beyond the scope of this work. Nonetheless, the discussion below aims to address a few key points regarding the *local* deposition kinetics for the purpose of further validating the model assumptions and discussing its limitations.

The model proposed here focuses on the transport of free radicals down the nanopores and their collisions with the pore wall along the way. Nevertheless, this model only implicitly incorporates the influence of monomers via sticking probability Γ (see Figure 4), which was assumed constant along the entire pore length. We acknowledge that this assumption was made to derive analytically tractable solutions. In our system, this assumption can be justified by the observation that DR_{norm} was primarily affected by P_I/P_I^{sat} but not P_M/P_M^{sat} (Figure 3), which supports the model's focus on the transport of free radicals.

That, however, may not be the case in systems where the rate of transport of monomers along a nanopore is considerably smaller than their maximum rate of consumption, for example, in the case of 1*H*,1*H*,2*H*,2*H*-perfluorodecyl acrylate (PFDA) monomers,[4] thus leading to an appreciable descending concentration gradient of monomers down the pore, or if a monomer-consumption-limited regime is in effect.[11] Nevertheless, this scenario could be addressed by combining the effective initiator concentration reported here with a previously reported reaction−diffusion model.[4] As such, a more general expression of local deposition rate as a function of depth along the pores can be achieved, which may enable predictions of local coating thickness and ultimately the conformality under nanoconfinement. Although an in-depth discussion on coating conformality is beyond the scope of this paper, we believe insights derived from the model could offer some interesting implications regarding conformality. For example, the model predicts that the effective concentration of free radicals would be subjected to the greatest amplification within a cylindrical nanopore of a few hundred nanometers long. One possible outcome of that is the enhanced termination of chain growth inside shorter nanopores or possibly near the entrance of a long nanopore, affecting coating conformality.

Future research will focus on the model development and validation that could account for local coating thickness. Such a model will provide insight into how the local amplification of effective initiator concentration under nanoconfinement, coupled with local monomer coverage variation, affects kinetics of initiation and termination, spatial variation of molecular weight, and coating thickness profiles along the ultrahigh-aspect-ratio nanopores. Future work may also focus on improving the molecular collision theories by considering diffuse reflection of the free radicals upon impinging the pore walls as well as radicals entering the pores via nonradial directions. From an experimental viewpoint, more precise thickness profile determination techniques and localized molecular weight measurements would be essential for validating such localized model predictions. Furthermore, experimental strategies that allow control over the direction or profile of radical flows could provide further validation to the collision model and thereby offer novel avenues for engineering coating thickness profiles. An intriguing question that arises from this model is how nanoconfinement geometries could influence the trajectory of the incident free radicals, their local effective concentrations, and the coating thickness profiles. For example, AAO pores with a closed bottom instead of an open exit may result in different deposition kinetics under the same deposition conditions, considering the flux of returning radicals under low-Γ conditions (see Figure 4B). Comparing kinetics and thickness profile obtained in nanoconfinement of various shapes (e.g., conical, spherical, and branched) may offer further insight into the geometry−trajectory−kinetics relationship. In the case of nanoconfinement with complex geometries beyond analytical tractability, *in silico* simulation methods such as direct Monte Carlo simulation[41] may shed light on the initiator transport and deposition kinetics.

4. CONCLUSIONS

To bridge the knowledge gap in nanoscale transport and polymerization kinetics, we performed a systematic experimental and theoretical investigation of polymer thin film growth under nanoconfinement. Conformal pHEMA thin films were deposited along the walls of ultrahigh-aspect-ratio nanopores. Our results showed that despite the slower rate of deposition inside the nanopores, which could be 94%−99% lower than that on a flat substrate, the rate followed the similar scaling laws with regard to P_M/P_M^{sat}. Nevertheless, the rate of deposition increased faster with P_I/P_I^{sat} under nanoconfinement than on a flat surface, until a plateau was reached. That distinct rate dependency on P_I/P_I^{sat} was attributed to the amplified radical−surface collisions due to the nanoconfinement, the theory of which was demonstrated by using a molecular collision model and validated by experimental data obtained macroscopically. The theoretical framework and experimental approach developed here could accelerate the precise surface engineering of nanostructured devices by offering insights into the reaction kinetics at the nanometer length scales, benefiting areas ranging from (bio)separation, (bio)sensing, and tissue engineering to energy harvest and storage.

■ ASSOCIATED CONTENT

Supporting Information

The Supporting Information is available free of charge at https://pubs.acs.org/doi/10.1021/acs.macromol.0c01534.

https://dx.doi.org/10.1021/acs.macromol.0c01534
Macromolecules XXXX, XXX, XXX−XXX

Derivation of DR_{pore} using the weight method and error propagation analysis on DR_{pore}; derivation of N_{pore} (with illustration) and η; finite element analysis of AAO membrane temperature under actual experimental conditions using COMSOL; validation of the weight method; validation of that simulation result by direct temperature measurement under the same conditions; additional SEM and AFM micrographs detailing the morphology of AAO membranes and Si wafer and coating conformality along AAO nanopores; relative areal collision frequency β as a function of pore diameter (PDF)

AUTHOR INFORMATION

Corresponding Author

Rong Yang − *Chemical and Biomolecular Engineering, Cornell University, Ithaca, New York 14853, United States;* orcid.org/0000-0001-6427-026X; Email: ryang@cornell.edu

Authors

Yifan Cheng − *Chemical and Biomolecular Engineering, Cornell University, Ithaca, New York 14853, United States;* orcid.org/0000-0003-2312-093X

Alexandra Khlyustova − *Chemical and Biomolecular Engineering, Cornell University, Ithaca, New York 14853, United States*

Pengyu Chen − *Chemical and Biomolecular Engineering, Cornell University, Ithaca, New York 14853, United States*

Complete contact information is available at: https://pubs.acs.org/10.1021/acs.macromol.0c01534

Author Contributions

Y.C. and A.K. contributed equally to this work.

Notes

The authors declare no competing financial interest.

ACKNOWLEDGMENTS

The authors thank the Office of Naval Research (ONR) for support through Award MURI N00014-20-1-2418 to R.Y. Analytical methods involved use of the Cornell Center for Materials Research (CCMR) Shared Facilities which are supported through the NSF MRSEC program (DMR-1719875). The authors thank Trevor B. Donadt and Prof. Donald L. Koch for helpful discussions.

REFERENCES

(1) Elam, J. W.; Routkevitch, D.; Mardilovich, P. P.; George, S. M. Conformal Coating on Ultrahigh-Aspect-Ratio Nanopores of Anodic Alumina by Atomic Layer Deposition. *Chem. Mater.* **2003**, *15* (18), 3507−3517.

(2) Wang, J.; Lin, Z. Freestanding TiO_2 Nanotube Arrays with Ultrahigh Aspect Ratio via Electrochemical Anodization. *Chem. Mater.* **2008**, *20* (4), 1257−1261.

(3) Chang, C.; Sakdinawat, A. Ultra-High Aspect Ratio High-Resolution Nanofabrication for Hard X-Ray Diffractive Optics. *Nat. Commun.* **2014**, *5* (May), 1−7.

(4) Asatekin, A.; Gleason, K. K. Polymeric Nanopore Membranes for Hydrophobicity-Based Separations by Conformal Initiated Chemical Vapor Deposition. *Nano Lett.* **2011**, *11* (2), 677−686.

(5) Tekin, H.; Ozaydin-Ince, G.; Tsinman, T.; Gleason, K. K.; Langer, R.; Khademhosseini, A.; Demirel, M. C. Responsive Microgrooves for the Formation of Harvestable Tissue Constructs. *Langmuir* **2011**, *27* (9), 5671−5679.

(6) Ozaydin-Ince, G.; Dubach, J. M.; Gleason, K. K.; Clark, H. A. Microworm Optode Sensors Limit Particle Diffusion to Enable in Vivo Measurements. *Proc. Natl. Acad. Sci. U. S. A.* **2011**, *108* (7), 2656−2661.

(7) Lachman, N.; Xu, H.; Zhou, Y.; Ghaffari, M.; Lin, M.; Bhattacharyya, D.; Ugur, A.; Gleason, K. K.; Zhang, Q. M.; Wardle, B. L. Tailoring Thickness of Conformal Conducting Polymer Decorated Aligned Carbon Nanotube Electrodes for Energy Storage. *Adv. Mater. Interfaces* **2014**, *1* (7), 1−6.

(8) Nejati, S.; Minford, T. E.; Smolin, Y. Y.; Lau, K. K. S. Enhanced Charge Storage of Ultrathin Polythiophene Films within Porous Nanostructures. *ACS Nano* **2014**, *8* (6), 5413−5422.

(9) Gleason, K. K. Chemically Vapor Deposited Polymer Nanolayers for Rapid and Controlled Permeation of Molecules and Ions. *J. Vac. Sci. Technol., A* **2020**, *38* (2), 020801.

(10) Donadt, T. B.; Yang, R. Vapor-Deposited Biointerfaces and Bacteria: An Evolving Conversation. *ACS Biomater. Sci. Eng.* **2020**, *6* (1), 182−197.

(11) Gleason, K. K. In *CVD Polymers: Fabrication of Organic Surfaces and Devices*; Gleason, K. K., Ed.; Wiley-VCH Verlag GmbH & Co.: Weinheim, 2015.

(12) Baxamusa, S. H.; Gleason, K. K. Thin Polymer Films with High Step Coverage in Microtrenches by Initiated CVD. *Chem. Vap. Deposition* **2008**, *14* (9−10), 313−318.

(13) Ozaydin-Ince, G.; Gleason, K. K. Tunable Conformality of Polymer Coatings on High Aspect Ratio Features. *Chem. Vap. Deposition* **2010**, *16* (1−3), 100−105.

(14) Baxamusa, S. H.; Gleason, K. K. Initiated Chemical Vapor Deposition of Polymer Films on Nonplanar Substrates. *Thin Solid Films* **2009**, *517* (12), 3536−3538.

(15) Gupta, M.; Gleason, K. K. Surface Modification of High Aspect Ratio Structures with Fluoropolymer Coatings Using Chemical Vapor Deposition. *Thin Solid Films* **2009**, *517* (12), 3547−3550.

(16) Ince, G. O.; Armagan, E.; Erdogan, H.; Buyukserin, F.; Uzun, L.; Demirel, G. One-Dimensional Surface-Imprinted Polymeric Nanotubes for Specific Biorecognition by Initiated Chemical Vapor Deposition (ICVD). *ACS Appl. Mater. Interfaces* **2013**, *5* (14), 6447−6452.

(17) Servi, A. T.; Guillen-Burrieza, E.; Warsinger, D. M.; Livernois, W.; Notarangelo, K.; Kharraz, J.; Lienhard V, J. H.; Arafat, H. A.; Gleason, K. K. The Effects of ICVD Film Thickness and Conformality on the Permeability and Wetting of MD Membranes. *J. Membr. Sci.* **2017**, *523*, 470−479.

(18) Nejati, S.; Lau, K. K. S. Pore Filling of Nanostructured Electrodes in Dye Sensitized Solar Cells by Initiated Chemical Vapor Deposition. *Nano Lett.* **2011**, *11* (2), 419−423.

(19) Hsieh, C. Y.; Lau, K. K. S. Growth of Polyglycidol in Porous TiO_2 Nanoparticle Networks via Initiated Chemical Vapor Deposition: Probing Polymer Confinement under High Nanoparticle Loading. *Adv. Mater. Interfaces* **2015**, *2* (17), 1−9.

(20) Chen, Z.; Lau, K. K. S. Suppressing Crystallinity by Nanoconfining Polymers Using Initiated Chemical Vapor Deposition. *Macromolecules* **2019**, *52* (14), 5183−5191.

(21) Lau, K. K. S.; Gleason, K. K. Initiated Chemical Vapor Deposition (ICVD) of Poly(Alkyl Acrylates): An Experimental Study. *Macromolecules* **2006**, *39* (10), 3688−3694.

(22) Lau, K. K. S.; Gleason, K. K. Initiated Chemical Vapor Deposition (ICVD) of Poly(Alkyl Acrylates): A Kinetic Model. *Macromolecules* **2006**, *39* (10), 3695−3703.

(23) Ozaydin-Ince, G.; Gleason, K. K. Transition between Kinetic and Mass Transfer Regimes in the Initiated Chemical Vapor Deposition from Ethylene Glycol Diacrylate. *J. Vac. Sci. Technol., A* **2009**, *27* (5), 1135−1143.

(24) Hanak, B. W.; Hsieh, C. Y.; Donaldson, W.; Browd, S. R.; Lau, K. K. S.; Shain, W. Reduced Cell Attachment to Poly(2-Hydroxyethyl Methacrylate)-Coated Ventricular Catheters in Vitro. *J. Biomed. Mater. Res., Part B* **2018**, *106* (3), 1268−1279.

(25) Christian, P.; Tumphart, S.; Ehmann, H. M. A.; Riegler, H.; Coclite, A. M.; Werzer, O. Controlling Indomethacin Release through

https://dx.doi.org/10.1021/acs.macromol.0c01534
Macromolecules XXXX, XXX, XXX−XXX

Vapor-Phase Deposited Hydrogel Films by Adjusting the Cross-Linker Density. *Sci. Rep.* **2018**, *8* (1), 1−12.
(26) Schneider, C. A.; Rasband, W. S.; Eliceiri, K. W. NIH Image to ImageJ: 25 Years of Image Analysis. *Nat. Methods* **2012**, *9* (7), 671−675.
(27) Yang, R.; Gleason, K. K. Ultrathin Antifouling Coatings with Stable Surface Zwitterionic Functionality by Initiated Chemical Vapor Deposition (ICVD). *Langmuir* **2012**, *28* (33), 12266−12274.
(28) Rasmussen, C. E.; Williams, C. K. I. *Gaussian Processes for Machine Learning*; The MIT Press: Cambridge, MA, 2006.
(29) Sulka, G. D. Highly Ordered Anodic Porous Alumina Formation by Self-Organized Anodizing; **2008**. 1.
(30) Lin-Vien, D.; Colthup, N. B.; Fateley, W. G.; Grasselli, J. G. *Infrared and Raman Characteristic Frequencies of Organic Molecules*; Elsevier: 1991.
(31) Pfluger, C. A.; Carrier, R. L.; Sun, B.; Ziemer, K. S.; Burkey, D. D. Cross-Linking and Degradation Properties of Plasma Enhanced Chemical Vapor Deposited Poly(2-Hydroxyethyl Methacrylate). *Macromol. Rapid Commun.* **2009**, *30* (2), 126−132.
(32) Martins, M. C. L.; Wang, D.; Ji, J.; Feng, L.; Barbosa, M. A. Albumin and Fibrinogen Adsorption on PU-PHEMA Surfaces. *Biomaterials* **2003**, *24* (12), 2067−2076.
(33) Perova, T. S.; Vij, J. K.; Xu, H. Fourier Transform Infrared Study of Poly(2-Hydroxyethyl Methacrylate) PHEMA. *Colloid Polym. Sci.* **1997**, *275* (4), 323−332.
(34) Chan, K.; Gleason, K. K. Initiated Chemical Vapor Deposition of Linear and Cross-Linked Poly(2-Hydroxyethyl Methacrylate) for Use as Thin-Film Hydrogels. *Langmuir* **2005**, *21* (19), 8930−8939.
(35) Elsner, G.; Kempf, J.; Bartha, J. W.; Wagner, H. H. Anisotropy of Thermal Expansion of Thin Polyimide Films. *Thin Solid Films* **1990**, *185*, 189−197.
(36) Hickey, G. S. Effect of Electron Radiation on Polymer Matrix Systems. *Thermochim. Acta* **1991**, *192*, 199−208.
(37) Ouyang, G.; Wang, C. X.; Yang, G. W. Surface Energy of Nanostructural Materials with Negative Curvature and Related Size Effects. *Chem. Rev.* **2009**, *109* (9), 4221−4247.
(38) Cardona-Martínez, N.; Dumesic, J. A. Acid Strength of Silica-Supported Oxide Catalysts Studied by Microcalorimetric Measurements of Pyridine Adsorption. *J. Catal.* **1991**, *127* (2), 706−718.
(39) Mao, Y.; Gleason, K. K. Hot Filament Chemical Vapor Deposition of Poly(Glycidyl Methacrylate) Thin Films Using Tert-Butyl Peroxide as an Initiator. *Langmuir* **2004**, *20* (6), 2484−2488.
(40) Servi, A. T.; Guillen-Burrieza, E.; Warsinger, D. M.; Livernois, W.; Notarangelo, K.; Kharraz, J.; Lienhard V, J. H.; Arafat, H. A.; Gleason, K. K. The Effects of ICVD Film Thickness and Conformality on the Permeability and Wetting of MD Membranes. *J. Membr. Sci.* **2017**, *523*, 470−479.
(41) Oran, E. S.; Oh, C. K.; Cybyk, B. Z. Direct Simulation Monte Carlo: Recent Advances and Applications. *Annu. Rev. Fluid Mech.* **1998**, *30* (1), 403−441.

https://dx.doi.org/10.1021/acs.macromol.0c01534
Macromolecules XXXX, XXX, XXX−XXX